J. Fluid Mech. (2008), *vol.* 616, *pp.* 419–443. © 2008 Cambridge University Press
doi:10.1017/S0022112008004072 Printed in the United Kingdom

The effect of confinement on the motion of a single clean bubble

B. FIGUEROA-ESPINOZA[1], R. ZENIT[1]†
AND D. LEGENDRE[2]

[1]Instituto de Investigaciones en Materiales, Universidad Nacional Autónoma de México,
Circuito Exterior s/n, Ciudad Universitaria, 04510 México, D.F., México
[2]Institut de Mécanique des Fluides de Toulouse, Alee du Prof. Soula, 31400 Toulouse, France

(Received 20 July 2007 and in revised form 1 September 2008)

The effect of confining a gas bubble between two parallel walls was investigated for the inertia-dominated regime characterized by high Reynolds and low Weber numbers. Single bubble experiments were performed with non-polar liquids such that the bubble surface could be considered clean; hence, shear free. The drag coefficient was found to be the result of two main effects: the Reynolds number and the confinement. The total drag could be written as the product of the corresponding unconfined drag, which depended mainly on the Reynolds number, and a function $F(s)=1+\kappa s^3$. The confinement parameter s was defined as the ratio of the bubble radius to the gap width. The value of the constant κ depended on the way in which the bubbles moved within the gap, which was found to be either in a rectilinear ($\kappa \approx 8$) or oscillatory trajectory ($\kappa \approx 80$). For $Re < 70$, and a range of values of the confinement parameter, the bubbles followed a rectilinear path. For this regime, numerical simulations were performed to obtain the drag force on the bubble directly; a reasonable agreement was found with experiments. Moreover, a comparison of these results with a potential-flow-based model indicated that the vorticity produced at the walls induced a significant part of the drag. For $Re > 70$, oscillations were observed in the bubble trajectory. In all cases, the oscillation occurred in a zigzag manner. Near the transition the bubbles oscillated but did not reach the walls; for larger Reynolds numbers, the bubbles collided repeatedly with the walls as they ascended. The instability, which is different from the well-known unconfined path instability, resulted from the reversal of sign of the wall-induced lift force: for low Reynolds number, the walls have a stabilizing effect because of the repulsive nature of the lift force between the walls and the bubble, while for high Reynolds number the lift is attractive and trajectories become unstable. Considering a model for the lift force of a bubble moving near a wall, the conditions for the transition were identified. A reasonable agreement between the model and experiments was found.

1. Introduction

The motion of bubbles rising through a liquid because of buoyancy has been the subject of numerous studies. This apparently simple phenomenon has shown to be of enormous complexity, reflected in a variety of different bubble shapes and trajectories ranging from simple rectilinear trajectories in the case of small spherical bubbles to

---

† Email address for correspondence: zenit@servidor.unam.mx

zigzag and helical paths in the case of oblate ellipsoidal bubbles (Clift, Grace & Weber 1978). The interest in understanding bubbly flows is widely justified by numerous engineering applications and natural phenomena. In most practical situations, bubbly flows are confined by walls. In particular, for the case of underground multiphase flow in oil and gas reservoirs, the fluid motion is restricted to very confined geometries in the interior of fractures or cracks. Paradoxically, most studies have been carried out for unconfined configurations.

The effect of confinement on the motion of submerged objects has been studied by many authors in the past. For the case of solid spheres and cylinders, exact analytical solutions for the case of creeping flow exist. Bairstow, Cave & Lang (1922) solved the creeping fluid motion around a circular cylinder confined between two parallel walls, considering a solution of the biharmonic equation. They found that the drag force was approximately 60 % larger than the unconfined case for $Re = 2aU\rho/\mu = 0.2$ and a confinement $s = a/W = 0.1$, where a is cylinder radius, U, its velocity, W the distance between walls and ρ and μ the fluid density and viscosity, respectively. Faxen (1922) calculated the drag force on a sphere moving confined between two parallel walls. He found that the drag force increases linearly with s. The motion of confined bubbles in the creeping flow regime can be solved by considering the solution for spheres and the Hadamard–Rybczynski drag correction (Hadamard 1911; Rybczynski 1911).

For high-Reynolds-number confined flows, there is no analytical expression for the drag experienced by a bubble moving between two vertical walls. The motion of a single bubble rising freely through a stationary liquid was studied by Levich (1948, 1962) and Moore (1963). Based on the boundary layer assumptions, Levich considered that the flow was essentially irrotational and that the drag could be calculated from the dissipation. In that way, an analytic expression for the drag coefficient, $C_D = 2F/(\rho U^2 \pi a^2)$, of a spherical bubble rising steadily through a quiescent liquid was found to be $C_D = 48/Re$. Moore (1963) analysed the same problem and showed that the velocity field to leading order could be considered to be irrotational or potential everywhere in the liquid, and that the correction to this was $O(Re^{-1/2})$ in the boundary layer of thickness $O(Re^{-1/2})$ near the surface of the bubble. Moore also showed that the wake behind the bubble was small, of size $O(Re^{-1/4})$, in contrast to the flow past a solid sphere for which there is a boundary-layer separation causing a finite region of recirculation. Moore (1965) extended his first study (Moore 1963) to ellipsoidal bubbles and showed that the drag coefficient depended strongly on the bubble aspect ratio, $\chi = R/r$, where R and r are the major and minor semi-axes of the bubble, respectively. He found that

$$C_{DMoore} = \frac{48}{Re} G(\chi) \left\{ 1 + \frac{H(\chi)}{Re^{1/2}} + O\left(Re^{-5/6}\right) \right\}, \tag{1.1}$$

where the function $G(\chi)$ is defined as

$$G(\chi) = \frac{1/3\chi^{4/3}(\chi^2-1)^{3/2}[(\chi^2-1)^{1/2} - (2-\chi^2)\sec^{-1}\chi]}{\left[\chi^2 \sec^{-1}\chi - (\chi^2-1)^{1/2}\right]^2}. \tag{1.2}$$

The function $H(\chi)$ does not have a closed form expression but is shown in table 1 of Moore (1965).

There are some analytical results for the drag and lift forces acting on a bubble moving parallel to a single wall. Van Wijngaarden (1976) and Biesheuvel & Van Wijngaarden (1982) used twin spherical expansions to calculate the velocity potential

	ρ (kg m^{-3})	μ (mPa s)	σ (mN m^{-1})	U (cm s^{-1})	a (mm)	$Re = 2aU\rho/\mu$	$We = 2aU^2\rho/\sigma$
Fluid 1	761	0.495	16.036	$10 < U < 23$	$0.20 < a < 0.7$	$90 < Re < 470$	$0.05 < We < 2.68$
Fluid 2	818	0.777	15.455	$5 < U < 22$	$0.25 < a < 0.7$	$40 < Re < 300$	$0.05 < We < 2.06$
Fluid 3	841	1.771	12.455	$3 < U < 18$	$0.15 < a < 0.7$	$30 < Re < 100$	$0.05 < We < 1.39$

TABLE 1. Fluid properties for all experiments.

of a pair of bubbles moving through a liquid at high Reynolds number. Using similar techniques, Kok (1993) calculated drag coefficient, C_D, for a pair of bubbles rising through a liquid, which is equivalent to the calculation of the drag of a bubble in the presence of a plane of symmetry or a virtual wall. He obtained

$$C_D = \frac{48}{Re}\left(1 + s^3 + \frac{3}{4}s^6 + \frac{11}{3}s^8 + \frac{39}{4}s^{10} + \cdots\right). \tag{1.3}$$

Here, $s = a/W$ is the ratio between the bubble radius and the distance between bubble centres W. Kumaran & Koch (1993) performed the same calculation, using a slightly different method, leading to the same result. As discussed by Faxen (1922), single wall calculations cannot be simply added to calculate the drag for the two-wall case, specially for small Reynolds number flows. Moreover, for the potential flow case, the addition of a second wall breaks the symmetry assumption and, therefore, the no-penetration condition at the solid wall is not satisfied.

For the case of confined bubbles, it can be argued that the total drag is the result of two separate effects: the flow around a corresponding freely rising bubble and the confinement effect. Legendre, Magnaudet & Mougin (2003) showed that for the case of two bubbles rising side-by-side, these two effects could be simply superposed to describe the total drag over the bubble. We will show that this superposition is also valid for the flow configuration studied here.

In this paper, the motion of a single clean slightly oblate bubble of equivalent radius a, rising through a quiescent liquid of dynamic viscosity μ and density ρ owing to buoyancy is studied. The bubble, moving at its terminal velocity, U, in the vertical direction, z, is confined between two parallel vertical walls separated by a distance W, as shown in figure 1. The drag coefficient will, therefore, depend on the dimensionless distance between walls $s = a/W$, that varies from $s = 0$ in the unconfined case to $s = 1/2$ in the most confined configuration when the walls contact the surface of the bubble on each side. The study focuses on the case for which inertial effects are bigger than viscous ones ($Re > 1$) and surface tension is dominant over inertia ($We = 2aU^2\rho/\sigma < 1$).

This study is mainly experimental. However, we have also used numerical simulations and analytical solutions to complete our investigation on the nature of the drag for confined ascending bubbles.

2. Experimental set-up

The experimental set-up is shown in figure 2. A thin channel was built using two glass sheets of approximately 20 cm width and 40 cm height, separated by a small gap. To vary the confinement, two nearly identical set-ups were used with gaps of 3.6 and 4.7 mm (measured with an accuracy of ±0.05 mm). At the bottom of the channel, bubbles were produced by blowing air through a capillary tube. The liquids used were silicon oil mixtures of different viscosities to avoid surface contamination.

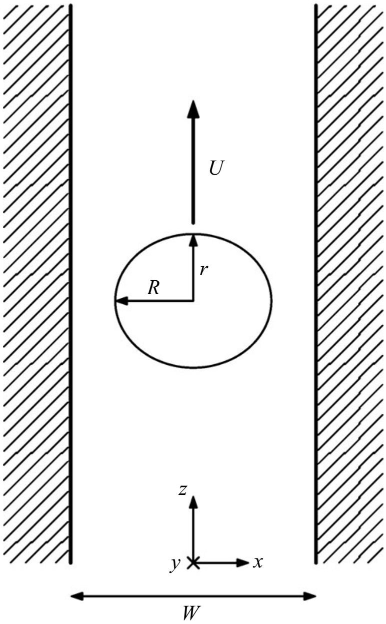

FIGURE 1. Bubble rising confined between two parallel walls.The coordinate system is shown.

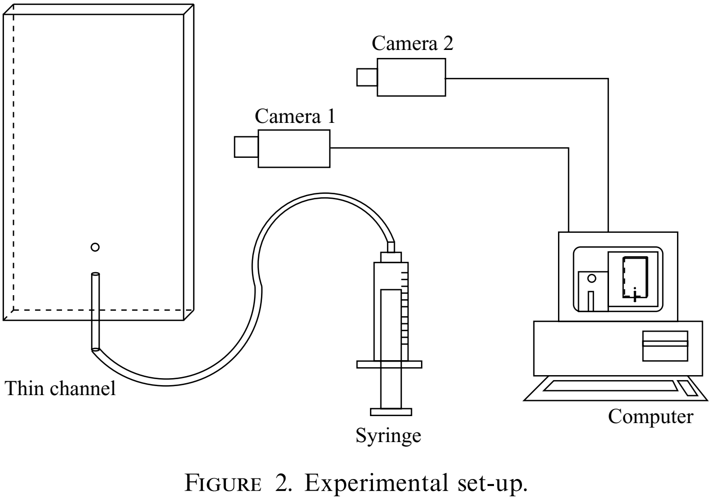

FIGURE 2. Experimental set-up.

The Reynolds number ranged between 30 and 500, while the Weber number was in the range of $0.05 \leqslant We \leqslant 2.7$. The verticality of the set-up was monitored with a digital level with an accuracy of 0.1 degrees. The properties of the liquids used are shown in table 1.

The shape and motion of the bubbles were captured using a high-speed camera and digital image processing software. The images were captured at approximately 10 cm from the capillary tip through the front wall (the y–z plane). The extent of the image was chosen in such a way as to maximize the relative size of the bubble in the digital image frame, taking into account the minimum distance that the bubble would travel before attaining its final velocity. This distance and the characteristic time needed to reach it can be estimated from a dynamic equation of motion obtained from a force balance between the Levich drag and buoyancy, considering the mass of the bubble to be the virtual mass, and neglecting the history force. The distance traversed by the bubble before attaining 95 % of the terminal velocity is approximately

$$L \approx 4.10 g\tau^2,$$

where $\tau = a^2\rho/(18\mu)$. For instance, for the largest bubble and the least viscous fluid in this investigation ($a = 0.7$ mm and $\mu/\rho = 0.65 \times 10^{-6}$ m^2 s^{-1}), L is approximately 70 mm. For smaller bubbles and more viscous fluids, this distance would decrease; hence, for all the tests in this investigation we can assume that the bubbles have reached their terminal velocity at the measuring point.

A second ordinary camera was used to measure the mean bubble velocity, by recording the bubble motion from a wider field of view that covered the length of the channel. The uncertainty in the measurements was less than 5 %. Once the distances and focus were calibrated, the rise velocity was measured using sequences of images. These images were digitally treated and transformed into binary images. A computer program was developed using the software Matlab to identify the bubble and measure its shape and velocity. To evaluate the effect of confinement on the drag coefficient, the terminal velocity U and the major and minor semi-axes, R and r, of the bubble were measured for different bubble sizes and wall separations. Most measurements were obtained by filming the motion of the bubbles through the front wall (in the y–z plane), i.e. the bubble motion across the gap was not recorded. The bubble equivalent radius, $a = (R^2 r)^{1/3}$, varied from 0.15 to 0.7 mm. The bubble aspect ratio $\chi = R/r$, ranged in between 1.0 and 1.7 for the conditions tested here. Bubble expansion as a result of its ascension through a pressure gradient can be shown to have an insignificant effect for this case; this effect was therefore neglected.

A few visualization experiments were performed using the high-speed camera and a mirror. The objective of this arrangement was to visualize the bubble motion both within the gap and across the width simultaneously (both x–z and y–z planes). Since in our set-up the width is approximately 50 times larger than the gap, the optical arrangement to obtain these images posed some challenges, resulting in poor spacial resolution. Although the images clearly show the nature of the motion for the different regimes, as will be shown below, they were not used to obtain quantitative measurements.

The drag coefficient was inferred from a steady vertical force balance between buoyancy and drag,

$$C_D = \frac{8}{3}\frac{rg}{U^2}. \tag{2.1}$$

As will be explained later, the drag coefficient was normalized with the corresponding drag coefficient of a freely rising ellipsoidal bubble of aspect ratio, χ, (Moore 1965):

$$C_D^* = \frac{C_D}{C_{DMoore}}, \tag{2.2}$$

where C_{DMoore} is defined in (1.2). By normalizing the drag coefficient in this way the effect of the confinement and that of the bubble shape are separated. Zenit & Magnaudet (2008) showed that Moore's expressions remain relatively accurate for Reynolds numbers as small as 50.

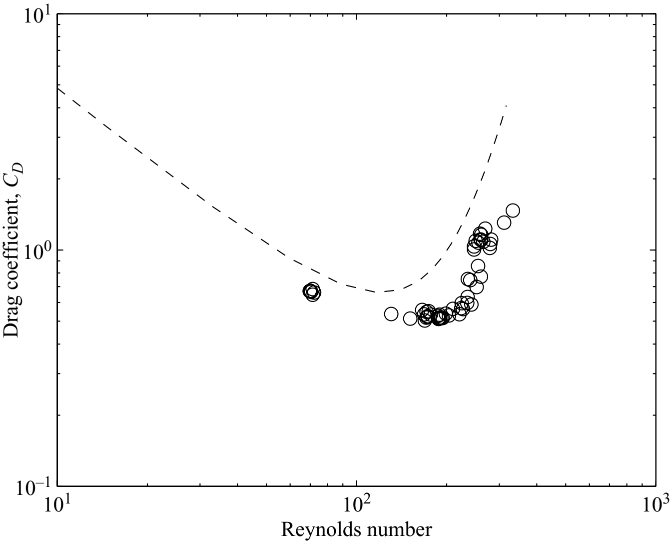

FIGURE 3. The drag coefficient as a function of Reynolds number for an unconfined bubble. Experimental measurements correspond to fluid 3 in table 1. The dashed line shows the prediction considering a clean ellipsoidal bubble (Moore 1965) for the corresponding physical properties of the liquid.

To corroborate that the gas–liquid interface of the silicon fluid was clean, the terminal velocity was measured for bubbles of different sizes in a large cylindrical container with a diameter of 10 cm. The experimental results are shown in figure 3. The measured drag coefficient is shown as a function of Reynolds number for the third fluid (see table 1). The experimental measurements are compared with the prediction of Moore (1965), which considers a clean ellipsoidal bubble. Clearly, the agreement between the experimental measurements and the model by Moore shows that the bubbles are moving as fast as the shear-free interface prediction. Note that, in fact, the drag coefficient measured is smaller than the theoretical prediction; in other words, the bubbles ascend faster than the prediction. This fact was also observed by Duineveld (1995) for the case of gas bubbles in hyper-clean water and by Zenit & Magnaudet (2008) for air bubbles ascending in silicon oils. The slightly larger velocities observed experimentally are probably the result of bubble shape, which is not exactly ellipsoidal in the experiments as assumed in the calculation of Moore.

The flow around clean bubbles, which is studied here, is amenable to potential flow theory treatment, as in Levich (1962). An analytical solution of the flow about a spherical bubble confined between two planes was obtained. Its development is shown in the Appendix. This solution will be compared with both experimental and numerical results in § 3.

In addition, to complement the experimental study presented here, direct numerical simulations of the flow around clean spherical bubbles were performed using the numerical code JADIM. This code has been extensively validated for several fluid dynamics problems in the past. Of particular relevance to the present context, we can refer to the study of a bubble in a simple linear shear flow (Legendre & Magnaudet 1998), the interaction of two bubbles (Legendre *et al.* 2003), and the effect of the

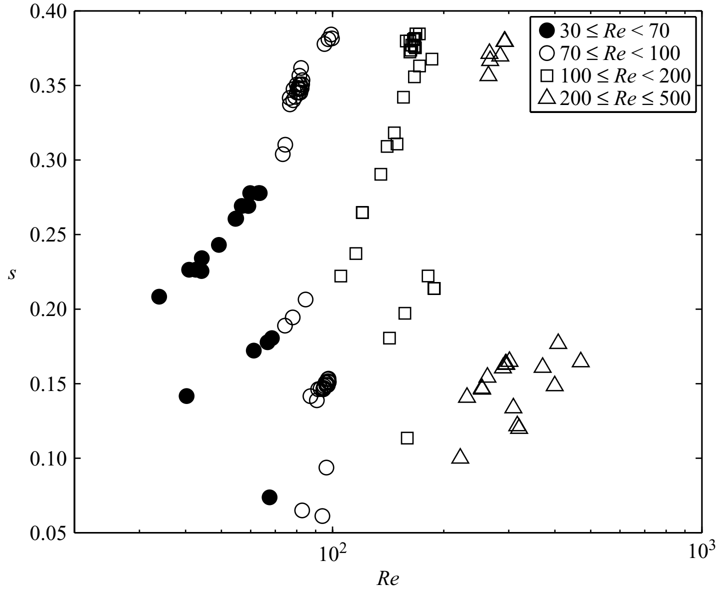

FIGURE 4. The normalized drag coefficient as a function of the confinement parameter. The solid and empty symbols show the experiments for which the trajectory of the bubble was found to be rectilinear and oscillatory, respectively. The empty circles show the experiments for which slight oscillations were observed (slightly above the threshold).

bubble deformation on the drag of a bubble (Legendre 2007). The code solves the full Navier–Stokes equations for a fluid with constant viscosity and density.

3. Experimental results: two types of bubble motion

Using the simple experimental set-up described above, many experiments were conducted to measure the terminal velocity of bubbles of different sizes considering the three different liquids listed in table 1. As the size of the bubble and the gap varied, the value of the confinement parameter, $s = a/W$, was changed.

The results of all the experiments conducted are shown in figure 4. The data are presented in terms of the confinement parameter, $s = a/W$, as a function of the Reynolds number. The movement of the bubbles in the channel was found to be strongly dependent on these two parameters. Two distinct behaviours were found. Bubbles ascended in a rectilinear manner, positioned in the centre of the channel for Reynolds numbers up to $Re \approx 70$. Above this critical value of the Reynolds number and for certain values of the confinement parameter, the bubble trajectories become oscillatory. For Reynolds numbers in between 70 and 100, that is at the onset of transition, only slight oscillations were observed: the bubbles moved back and forth within the gap without touching the walls. For larger Reynolds number, the bubbles bounced against the walls during their ascension. In the figure, the data are separated into rectilinear and oscillating trajectories.

Figure 5 shows typical photographs of the two behaviours. To observe the bubbles from the front and side simultaneously, these images were captured by the high-speed camera and a mirror. Figure 5(*a*) shows a superposition of images of the same bubble

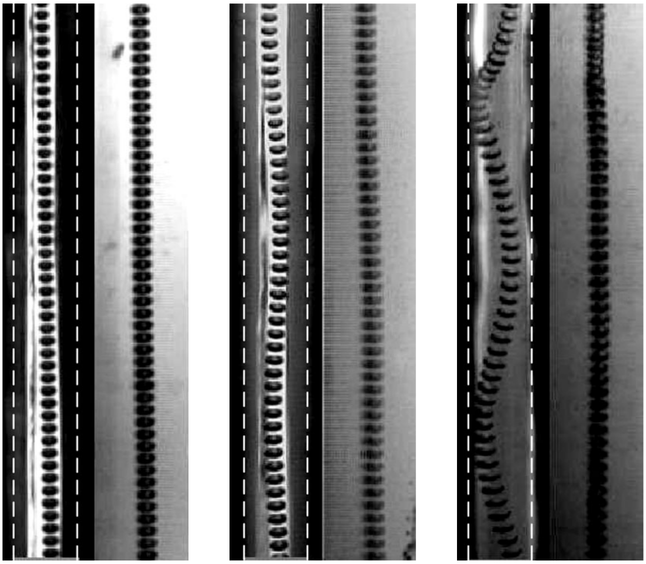

(*a*) (*b*) (*c*)

FIGURE 5. Bubble ascending in the confined channel. The motion is viewed from both sides at once (narrow and wide dimensions, on the left and right, respectively). The bubble is shown at different time instants ($\Delta t = 4$ ms) in the same plate: (*a*) Straight trajectory, $Re \approx 60$, $s \approx 0.13$, (*b*) slight zigzag trajectory, $Re \approx 100$, $s \approx 0.13$ and (*c*) zigzag trajectory, $Re \approx 300$, $s \approx 0.13$. The vertical dashed lines show the approximate position of the walls. In all cases shown, $a \approx 0.65$ mm and $W = 4.7$ mm. The aspect ratio varies approximately from 1.2 to 1.6, from case (*a*) to (*c*).

at different time instants showing that the bubble rises straight in the centre of the channel, which corresponds to a small Reynolds number case. Figure 5(*b*) shows a bubble rising at a Reynolds number slightly larger than the transition value. From the two perpendicular views, it can be seen that the oscillation takes place only in one direction, i.e. in a zigzag path within the gap (viewed from the front of the channel). The magnitude of the oscillation remains small. Figure 5(*c*) shows the trajectory of an oscillating bubble for a larger Reynolds number. In this case, the bubble moves and collides against the walls. During the collision a strong reduction of the velocity is observed, which results in larger fluctuations and a smaller mean.

Interestingly, the transition to an oscillatory trajectory occurs at a Reynolds number which is much smaller than a freely rising isolated bubble (about 660 for pure water (Duineveld 1995) and from 100 to 400 for silicon oils of decreasing viscosity (Zenit & Magnaudet 2008)), and also at a smaller aspect ratio (about 2.0 for water and silicon oils (Zenit & Magnaudet 2008)). For the case of isolated bubbles the oscillatory trajectory is the result of the instability of the wake, which is directly linked to the amount of vorticity produced on the bubble surface. As will be shown later, the source of the instability of the trajectory is completely different in this case. To present the results clearly, we have opted to separate them into rectilinear and oscillating trajectories.

4. Bubbles moving in a rectilinear trajectory

The experimentally determined drag for bubbles ascending in a rectilinear trajectory is presented in figure 6. The vertical axis represents the normalized drag, C_D/C_{DMoore},

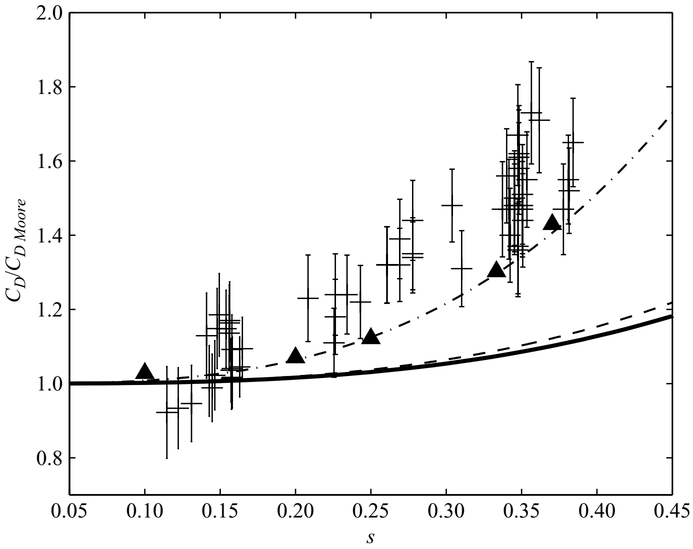

FIGURE 6. Normalized drag coefficient as a function of the confinement parameter. The plus signs (with error bars) show the experimental results. The solid triangles show the simulation results. The solid and dashed lines show the analytical results of (4.1) and (4.2), respectively. The dashed–dotted line shows the fit of the simulation results given in relation (4.3).

and the horizontal axis corresponds to the dimensionless distance between walls, s. The experimental data correspond to a range of Reynolds numbers between 30 and 70 approximately. For these experiments, the bubble remains at the centre of the channel. As s increases from $s=0$ (unconfined case, where the normalized drag tends to unity) to $s=1/2$ (the most confined configuration), the drag increases monotonically reaching nearly two times the unconfined drag.

We can now compare the experimental results with the analytical expression for the confined drag obtained from potential flow theory. This calculation is described in detail in the Appendix. It considers the motion of a spherical bubble confined by two virtual walls. The normalized drag from this calculation is (A 30)

$$\frac{C_D}{C_{D\,Levich}} = 1 + 2s^3 + \frac{17}{8}s^6 + O(s^8) + \cdots . \tag{4.1}$$

Note that in this case the drag coefficient was normalized by $C_{D\,Levich}$ which is the corresponding unbounded situation for $\chi=1$. The prediction of this expression is also shown in figure 6 along with the experimental data. Clearly, for values of the confinement parameter greater than 0.15, the analytic prediction significantly underestimates the value of the drag. This is, however, expected because the calculation of the drag does not account for the non-slip condition on the walls. If the infinite series of dipoles is considered, the normalized drag is (A 35)

$$\frac{C_D}{C_{D\,Levich}} = 1 + 2\zeta(3)s^3 + \cdots = 1 + 2.3s^3 + \cdots , \tag{4.2}$$

where ζ is the Riemann–Zeta function. This solution is also far from the experimental measurements when the value of the confinement is significant. As will be discussed later, the vorticity produced at the wall cannot be neglected; this is the reason why the potential flow underestimates the drag. Vorticity has a key role on the dissipation, and hence on the drag (Legendre 2007).

To explore further the nature of the drag increase resulting from confinement, we complemented our experimental investigation with numerical simulations of the same flow. The details of the simulation code can be found in Legendre *et al.* (2003) and are left out for brevity. The flow of a static spherical bubble placed in between two moving walls is considered. The drag force on the surface of the bubble was measured directly by integrating the total stress on the surface of the bubble. Simulations to evaluate the effect of confinement were obtained by varying the value of s in the range $0.05 < s < 0.38$. These results are compared with experiments and the potential flow solution in figure 6. The normalized drag from the numerical simulations is calculated as $C_D/C_{Ds\to 0}$. Despite the scattering of the experimental results, it can be observed that the simulation results are in reasonable agreement with the experiments. For most experiments the drag coefficient is slightly larger than the numerical results. Note that for the range $0.1 < s < 0.2$ some values of the normalized drag are smaller than one; these are clearly indicative of experimental uncertainty since the normalized drag for an unconfined bubble should be unity. The analysis of the numerical results shows that the drag dependency is also proportional to s^3. The drag obtained numerically can be closely fitted to

$$\frac{C_D}{C_{Ds\to 0}} = 1 + 8s^3 + O(s^4). \tag{4.3}$$

Note that the s^3 dependency was also obtained from the potential flow solution; the expression fitted to the numerical results indicates that the viscous effect is four times the potential prediction. In the next section, we analyse the increase of drag with confinement considering the value of the maximum vorticity produced on the walls.

4.1. *The relation between vorticity production and the drag*

Recently, Legendre (2007) argued that the drag force for Stokes flows can be expressed as a function of the maximum vorticity Ω_{max} as

$$D = -4\pi\mu a^2 \Omega_{max}. \tag{4.4}$$

Legendre also extended this relationship to the case of large Reynolds numbers, observing that a substitution of the maximum vorticity $\Omega_{max} = 3U/a$ into the Levich drag, $D = -12\pi\mu a U$, gives the same result as in the above equation. Legendre performed numerical simulations to verify that this holds true for intermediate values of the Reynolds number up to 500. The drag force (4.4) in dimensionless terms, that is the drag coefficient, can be obtained as a function of the maximum vorticity

$$C_D = \frac{16}{Re}\frac{a}{U}\Omega_{max}. \tag{4.5}$$

Let us consider a global momentum balance for a steady confined bubble flow

$$\Delta\rho g \frac{\pi d^3}{6} = -F_D + \int_{wall} \tau_{xy}\, \mathrm{d}S, \tag{4.6}$$

where τ_{xy} is the shear stress on the wall. Note that τ_{xy} can also be expressed as a function of the wall vorticity Ω_{wall}, $\tau_{xy} = \mu\Omega_{wall}$. The left-hand side of (4.6) is in fact the drag force of an unconfined bubble, $F_{D\infty} = -\Delta\rho g \pi d^3/6$. Therefore, we can write

$$F_D = F_{D\infty} + \int_{wall} \mu\Omega_{wall}\, \mathrm{d}S \tag{4.7}$$

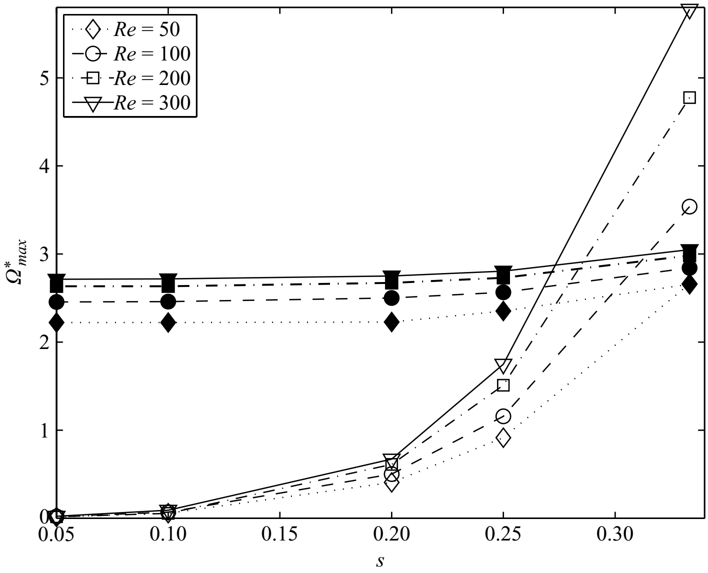

FIGURE 7. Maximum normalized vorticity Ω^*_{max} as a function of the confinement s for different values of the Reynolds number. The solid and empty symbols show the bubble and wall maximum vorticity, respectively.

showing that the drag is additive and its increase is proportional to the vorticity produced on the wall.

To estimate the contribution of the wall vorticity for different values of the confinement, s, the maximum normalized vorticity $\Omega^*_{max} = \Omega_{max} a/U$ was calculated from the numerical simulation results. Figure 7 shows a comparison between the maximum vorticity measured at the bubble surface and at the wall. It can be observed that the increase in the maximum vorticity in the surface of the bubble is not substantial compared to that of the wall. More importantly, by plotting the data in a log–log scale, it can be shown that the wall vorticity also increases proportionally to s^3.

Since the vorticity produced on the walls is known, an estimation of the drag increase can be obtained. In fact, the drag predicted from potential flow theory can be corrected, adding this effect. However, before attempting that, it must be noted that the bubbles in the experiment are not very oblate (aspect ratio slightly larger than unity, $\chi < 1.1$, for rectilinear trajectories). Based on the results of Legendre (2007), we can argue that for such small values of χ, the effect of the bubble shape is not very significant in the total confined drag.

4.2. *An estimation of the confined drag*

To estimate the drag on a confined bubble, we consider an additive contribution of the potential flow estimation with the drag resulting from the vorticity generated at the wall. This assumption is appropriate in view of the argument leading to (4.7). Therefore, we can write

$$\frac{C_D}{C_{DMoore}} = 1 + 2s^3 + \frac{16\Omega^*_{max}}{Re}, \tag{4.8}$$

where $\Omega^*_{max} = \Omega_{max} a/U$. From the experiments, Re and χ can be obtained and therefore the confined can be estimated.

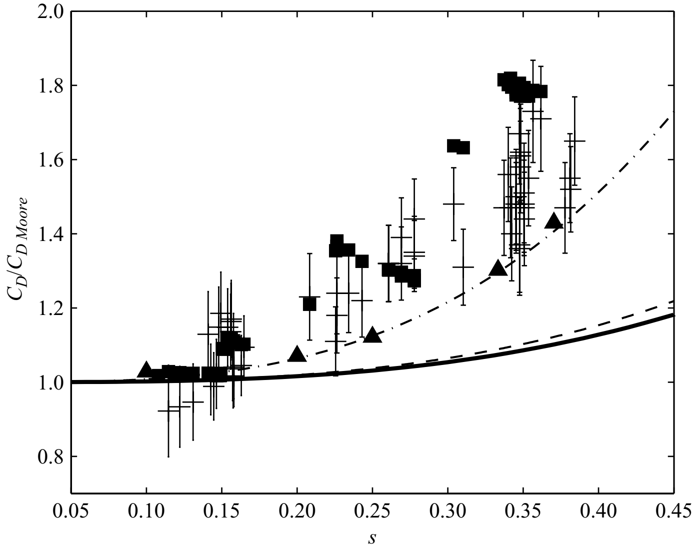

FIGURE 8. Normalized drag coefficient as a function of the confinement parameter, s. The symbols are the same as in figure 6. The additional symbols, solid squares, are the estimates of the drag considering (4.8).

This estimate is plotted in figure 8 where the experimental and numerical results are also presented. The agreement is good without any additional parameter fitting. Clearly, since the comparison is good, the value of the contribution of the term $(16\Omega^*_{max})/Re$ is approximately $6s^3$. Hence,

$$\Omega^*_{max} \approx \frac{3}{8} s^3 Re. \tag{4.9}$$

The functional dependence is correct considering that the maximum wall vorticity does increase as s^3, as shown in figure 7.

5. Bubbles moving in an oscillating trajectory

As already mentioned in § 1, when a single air bubble rises through a liquid driven by buoyancy, its trajectory can either be rectilinear or oscillating, depending on the values of the relevant parameters (Clift *et al.* 1978). The transition from rectilinear to oscillating trajectory has been studied by many researchers (see Veldhuis 2007 for a recent account). It has been reported that for air bubbles in ultrapure water, the onset of this transition occurs at Reynolds number of approximately 660, Weber number of approximately 3, and aspect ratio of 2.0 (Duineveld 1995). Nevertheless, small amounts of surface contamination can dramatically lower this threshold to Reynolds numbers of approximately 200. Recently, Zenit & Magnaudet (2008) showed that for other clean liquids, the transition to oscillatory trajectories did not only depend on the Reynolds number, but also on the bubble aspect ratio. It has been demonstrated that the reason for this phenomenon is the instability of the vorticity structure in the wake behind the bubble (Magnaudet & Mougin 2007; Yang & Prosperetti 2007), which in turn generates a horizontal force (lift) that causes the sideways motion of the bubble (Shew, Poncet & Pinton 2006).

De Vries (2001) and more recently Veldhuis (2007) analysed the wake structure of oscillating bubbles through Schlieren images of wake structures for straight and zigzagging bubbles. The wake of the latter presented two long thin counter-rotating vortices, which had also been described by the numerical simulations of Mougin & Magnaudet (2002). The mechanisms that make a bubble deviate from a rectilinear trajectory can be summarized as follows: the double-threaded vortex structure that appears behind the bubble produces a lift force. As the angle between the path and vertical grows, the driving force (buoyancy) decreases and so does the velocity. At lower speeds the bubble cannot maintain the wake production, so the path curvature decreases and the wake dissipates. Since the lift vanishes under these conditions, the bubble starts accelerating due to buoyancy and the cycle starts again with a vorticity sign reversal. This would anticipate a somewhat intermittent wake structure when path instability occurs. Direct observations of the wake structures by Brücker (1999) support this hypothesis.

For the case of confined bubbles the onset of oscillations has not been studied to date. We observe that bubbles begin to deviate from a rectilinear trajectory for certain values of the Reynolds number and the confinement parameter. The onset occurs at Reynolds numbers and aspect ratios much lower than those corresponding to unconfined path instability. The trajectories were in a zigzag manner, not spiral, for Reynolds number of approximately 70. For higher Reynolds numbers, the bubbles were attracted towards the walls and in some cases bounced back and forth from one wall to the other.

5.1. *The drag for bubbles with path oscillations*

In the same channel, experiments were performed with bubbles in which path oscillations were observed. The drag was measured using the mean vertical rise velocity $\bar{U}$, using (2.1). Figure 9 shows the evolution of vertical rise velocity with position and the bubble trajectory. The two cases shown correspond to the images shown in figure 5 for the oscillating trajectories. In case (*a*), corresponding to the slight oscillation case, the amplitude of oscillation is small compared to the channel width; the bubble does not reach either wall and the velocity does not change significantly. Since the bubble is ascending near the transition from wall-repulsion to wall-attraction, it is possible that the sign of the lift force changes as the bubble translates within the gap, causing oscillations that do not result in wall collisions. However, for case (*b*), the bubble moves across the whole gap experiencing cycles of acceleration and deceleration while ascending. The fluctuations are of significant magnitude. These arise because of the horizontal motion of the bubble and the collisions of the bubble with the walls. In the figure, a collision can be observed at $z/W \approx 0.70$; the vertical velocity decreases significantly during the contact with the wall reaching a value of $0.75U$. The significant decrease of velocity during the approach–contact–rebound process was discussed by Moctezuma, Lima-Ochoterena & Zenit (2005) and earlier by De Vries (2001). As a result of each collision, the bubble velocity changes significantly leading to an increased level of fluctuations which in turn causes an increase of the mean drag. As a result of the collision of a bubble with a vertical wall, it is possible to have a normal restitution coefficient larger than unity (Sato *et al.* 2007) for certain conditions (resulting from a transfer from the vertical momentum to the horizontal momemtum). In other words, the rebound velocity would be larger than the approach velocity in the normal direction. Therefore, due to this interaction, it is possible for a bubble to travel from one wall to the other and collide successively with both walls while ascending.

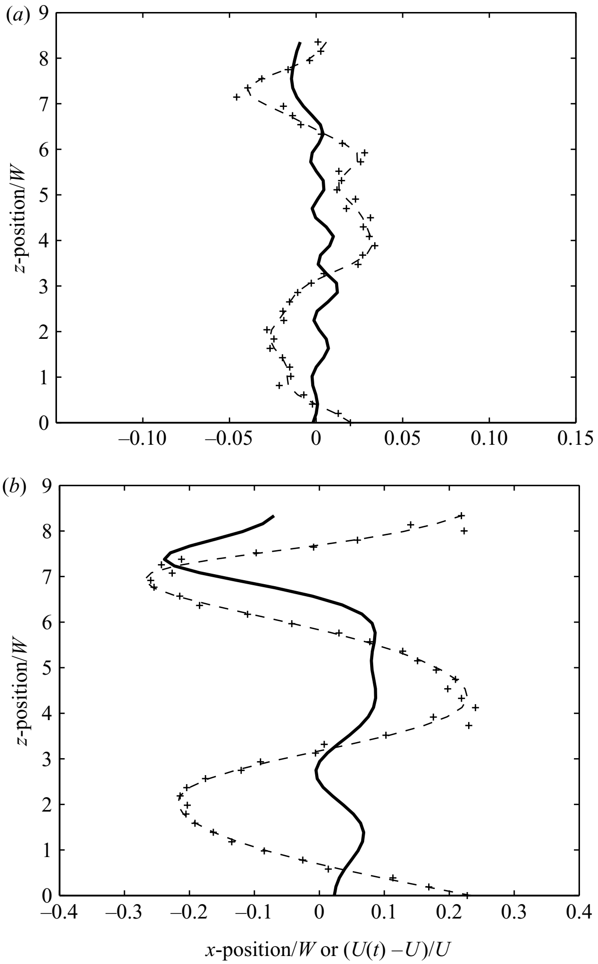

FIGURE 9. Trajectories and vertical velocities of two oscillating bubbles ascending in the confined channel. The plus signs show the x–z position of the bubble, normalized by the channel width, W; the dashed line shows a fit of the bubble position; the thick solid line shows the difference between the instantaneous velocity and the mean vertical rise velocity, normalized by U: (a) slight zigzag trajectory, $Re \approx 100$, $s \approx 0.13$ and (b) zigzag trajectory, $Re \approx 300$, $s \approx 0.13$. Cases (a) and (b) correspond to images (b) and (c) of figure 5.

The effect of the oscillations on the drag is illustrated in figure 10, where the normalized drag coefficient C_D^* is plotted for different values of s. Measurements for non-oscillating bubbles (already shown in figure 6) are also shown for comparison. The drag is much larger for the oscillating case, reaching almost three times the corresponding value for the same s. The dispersion of the data is also higher in the oscillating case due to enhanced velocity fluctuations. The oscillating phenomenon restricts the possibility of comparing the experimental results with those obtained numerically or theoretically.

Interestingly, the normalized drag for oscillating bubbles can be approximately fitted to

$$\frac{C_D}{C_{DMoore}} \approx 1 + 80 s^3. \tag{5.1}$$

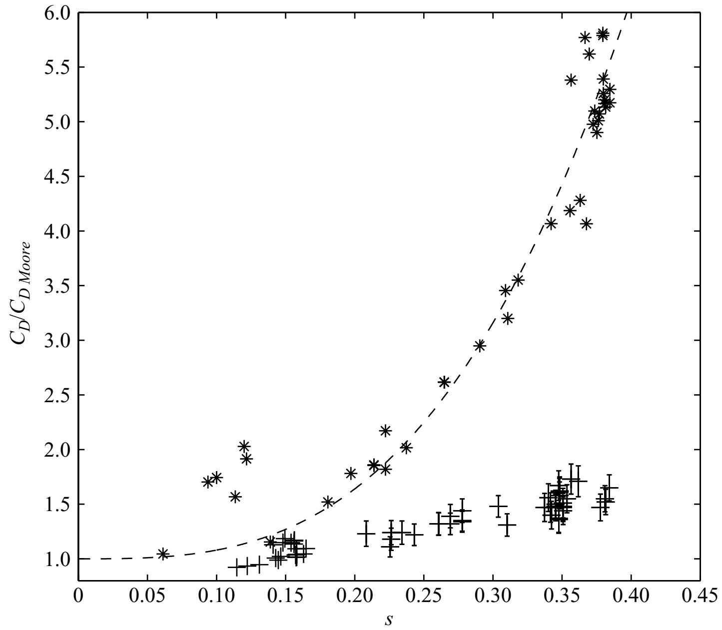

FIGURE 10. Normalized drag as a function of s for bouncing bubbles. The asterisks show the experiments for which the trajectory was found to be oscillating. The dashed line is a best fit for all the experiments, (5.1). The experiments for which rectilinear trajectories were observed are also shown for comparison.

Although the bubbles undergo collisions and consecutive cycles of deceleration and acceleration, the functional dependence of s^3 is retained.

We can now attempt to estimate the confined drag for oscillating bubbles, considering the results obtained for rectilinear bubbles. For that case we found that $C_D^* \approx 1+8s^3$. The number 8 in front of s^3 can be thought as the half contribution from each wall:

$$C_D^* \approx 1 + \frac{1}{2}\frac{k^3}{y_1^3} + \frac{1}{2}\frac{k^3}{y_2^3} = 1 + \frac{1}{2}k^3\left(\frac{1}{|y_1|^3} + \frac{1}{|y_2|^3}\right), \tag{5.2}$$

where y is the horizontal distance within the channel, such that $y_1 + y_2 = W$ for $s = a/W$. We can consider a simplified case in which the bubble is no longer in the centre of the channel, but moves vertically with a sinusoidal horizontal motion

$$y_2 = \frac{W}{2} - \frac{W-a}{2}\cos(\omega z), \tag{5.3}$$

where z is the vertical coordinate. An average drag coefficient can be calculated for a bubble undergoing one quasi-static oscillation cycle:

$$\langle C_D^* \rangle = \frac{1}{L}\int_0^L C_D^* \,\mathrm{d}z \tag{5.4}$$

with $\omega L = 2\pi$. Therefore,

$$\langle C_D^* \rangle = 1 + \frac{8s^3}{2\pi}\int_0^{2\pi} \frac{\mathrm{d}z'}{|1-(1-2s)\cos(z')|^3} = 1 + 8s^3 I(s), \tag{5.5}$$

where the function $I(s)$ can be integrated numerically for different values of s. Considering the limit $s \rightarrow 0$, $I(0) = 5/2 + O(s)$ which implies that

$$\langle C_D^* \rangle \sim 1 + 20s^3. \tag{5.6}$$

For increasing values of s the function $I(s)$ decreases, which would lead to a smaller coefficient in front of s^3. The model correctly predicts the dependence of C_D which is an indication that such a dependence is a result of the motion of the bubble within the channel gap. However, a more accurate prediction is not possible with this simple model. Although it accounts for the motion of the bubble within the gap, it does not account for the deceleration–acceleration process that the bubble experiences when a collision with the wall occurs. To include the effect of this process is not simple and it will not be attempted here. It is clear, however, that a significant part of the increased drag on oscillating bubbles arises because bubbles are colliding with the walls.

Based on these results, it can be argued that the drag increase is a result of three main mechanisms: increased bouncing (coefficient of restitution greater than 1) due to a transfer of vertical to horizontal (Sato *et al.* 2007); additional vorticity produced and shed during each wall-interaction event (De Vries 2001) and the additional dissipation in the film formed in between bubble and wall during the interaction. We argue that all these mechanisms can be related to the increased value of the drag measured for the case of zigzagging confined bubbles.

6. Wall instability

It was observed experimentally that the presence of the walls induced the zigzagging motion at smaller values of the Reynolds number and deformation than expected from the point of view of the well-known *unconfined* path instability. This fact can be explained in terms of the lift on the bubble caused by the walls. The presence of a wall near a rising bubble has already been analysed by several authors. In particular, Takemura & Magnaudet (2003) compiled several previous studies with their own measurements and composed an expression for the lift force based on experimental, theoretical and numerical grounds (taking into account both the low and high Reynolds number limit cases and the dynamic effects of vorticity). The resulting lift is dependent on the distance to the wall and the Reynolds number. More importantly, the sign of the lift force was found to change from being wall-repulsive to wall-attractive as the Reynolds number increased. This dependency can be explained as follows: for low Reynolds numbers, viscous forces are dominant over inertial ones, and the resulting lift force between bubble and wall is repulsive (Happel & Brenner 1991), while for high Reynolds numbers the dominant forces are inertial in nature, and the resulting lift force is attractive (Van Wijngaarden 1976). Legendre *et al.* (2003) studied the interaction between two horizontally aligned bubbles where the same type of reversal of the lift force was observed.

To understand the transition from rectilinear to zigzagging trajectories in our case, let us now consider a bubble rising between two vertical walls at low Reynolds number: if its trajectory deviates from the centreline between the walls, the repulsive forces from both walls would tend to repel the bubble back to the centreline. This stabilizing effect makes it reasonable to expect that the confined rectilinear trajectory would be stable for low Reynolds numbers. On the contrary, if the bubble rises at high Reynolds number between the walls, the lift is attractive. If a small perturbation is imposed, the bubble will move slightly from the centreline and the attraction towards

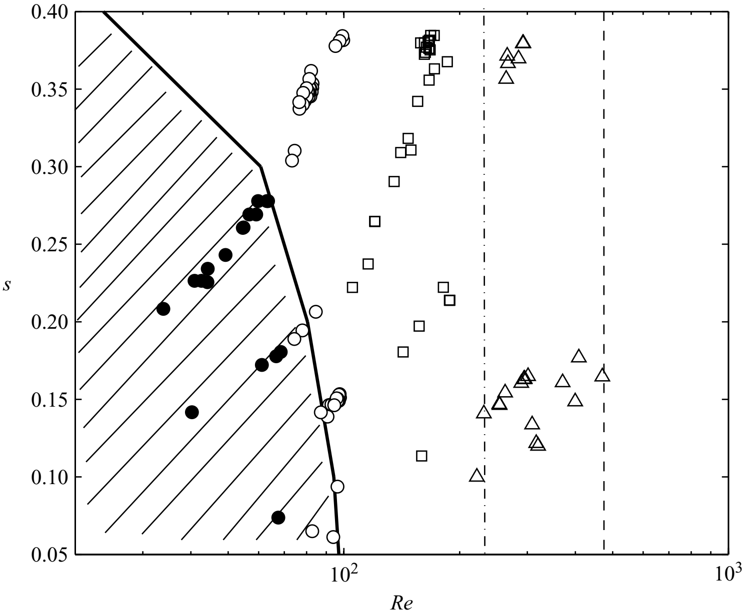

FIGURE 11. Regions of stability in the *Re*–*s* plane. The symbols show all the experiments performed in this investigation: •, $30 < Re < 70$; ∘, $70 < Re < 100$; □, $100 < Re < 200$ and △, $200 < Re < 500$. The vertical lines show the approximate value of the Reynolds number for Fluid 1 (dashed line) and Fluid 3 (dashed dotted line). The solid curve shows the calculation of zero lift force superposing the effect of two walls, considering the expression proposed by Takemura & Magnaudet (2003). The dashed region show the region of stability (wall-repulsive region).

the walls will tend to drift the bubble farther away from the centreline, having as a result a destabilizing effect. Near the transition, the nature of the horizontal force may change (attractive or repulsive) as the bubble moves within the channel, resulting in slight oscillations.

To test this hypothesis, a plot of s as a function of Reynolds number was composed. Figure 11 shows regions of stability for different cases: the onset of unconfined path instability for the case of fluids 1 and 3 (from table 1) are located at $Re \approx 470$ and $Re \approx 210$, according to Zenit & Magnaudet (2008). In the figure, the experiments shown as empty circles showed slight oscillations, and we considered them to be at the onset of the transition. The solid circles show experiments for which only rectilinear paths were observed.

To estimate the zero-lift contour in the *Re*–*s* plane, we considered the following: the expression proposed by Takemura & Magnaudet (2003, equation (6*a*)) was used to superpose the lift experienced by a bubble located at a position slightly eccentrical (say, $W/2 + \epsilon$ from one wall and $W/2 - \epsilon$ from the other one). The corresponding lift forces were added, resulting in a total lift force that could be directed either to the centre or against the walls. If the superposed lift is directed to the centre, then the bubble trajectory is stable for those specific values of the Reynolds number and s. The region in the *s*–*Re* plane where a sign reversal occurs for this 'two-wall' lift corresponds then to the zero lift contour. We verified that the shape of the contour did not change appreciably for values of ϵ/s in between 0.001 and 0.3. This contour is presented in figure 11 as a solid line. To the right (respectively left) of this line, the centre position of the bubble is unstable (respectively stable). Although the superposition of the lift of two walls is not exact, the resulting contour is in close agreement with our experimental observations. The superposition can be justified for large Reynolds number, where the interactions are not of long range as is the case for viscous flows. Note that above a certain value of the confinement (between $s = 0.4$ and $s = 0.45$), all bubbles are predicted to be unstable; however, the precision of the superposed contour cannot be expected to be good at high confinements.

7. Summary and conclusions

The effect of confinement on the drag coefficient of ascending clean bubbles was studied. Our experimental results showed that the dimensionless drag force depended on two different parameters: the Reynolds number and the dimensionless distance, $s = a/W$. An expression for the drag coefficient was obtained as the product of the unconfined drag, which depended on the Reynolds number, and a function $F(s)$. For small values of the Reynolds number ($Re < 70$), it was found that the function $F(s) \approx 1 + 8s^3$. This dependence coincided with the fact that bubbles ascended in a rectilinear manner. In this regime, the induced lift force is wall-repulsive which maintains the bubble in a stable position in the centre of the gap. Furthermore, for this low Reynolds number case, the function $F(s)$ was found to be the result of viscous and inviscid contributions. The inviscid contribution was obtained by calculating the drag on a sphere in between two virtual vertical walls in a potential flow formulation. The viscous contribution was inferred from the wall vorticity, obtained from direct numerical simulations of the flow. For Reynolds numbers larger than 70 and some values of s, the trajectory of the bubble was found to occur in a zigzag manner, evolving from slight to strong oscillations as the Reynolds number increased. For $70 < Re < 100$, the bubbles moved within the channel gap without touching the wall. For larger Reynolds number, the bubbles were observed to undergo repeated collisions as they ascended. The collisions were characterized by periods of strong deceleration–acceleration, which resulted in large values of fluctuations and a smaller mean velocity. The unstable trajectory was found to result from the wall-attractive nature of the induced lift on the bubble. Surprisingly, the drag coefficient was found to preserve the same functional dependence on s. For this case, $F(s) \approx 1 + 80s^3$. Clearly, the larger value of the factor in front of s^3 indicates an increased drag as the confinement becomes larger when the bubbles oscillate. In this regime, a significant part of the drag is a result of the bubble collisions with the confining walls.

Considering the expression of the wall-induced lift on a bubble by a *single* wall from Takemura & Magnaudet (2003), a model was composed to calculate the two-wall lift. The conditions for the transition between wall-repulsive to wall-attractive were calculated and compared with the experimental results. The comparison was remarkable despite the effect of each wall being simply added.

The path instability observed in this study is different from that observed in freely rising bubbles. The difference lies in the fact that in the confined case there is a strong wall influence. The oscillations have a strong effect on the drag, causing it to increase considerably. It would be interesting to investigate the confinement effects on bubbles which oscillate if unconfined. For such a case, a complex interaction between wake- and wall-induced forces can be envisioned. This study will be undertaken in the future.

B. Figueroa-Espinoza acknowledges the financial support from Conacyt and DGEP-UNAM for his graduate studies. R. Zenit thank the PASPA-DGAPA program of UNAM for supporting his sabbatical stay at the IMFT, France. The authors also thank Araceli Ordóñez Medrano for her help with the the surface tension measurements.

Appendix. Potential flow calculation of the drag on a bubble confined between two vertical walls

With the assumptions of $Re \gg 1, We < 1$ a potential flow formulation for the external velocity field around the bubble can be considered. If the potential function is known analytically, then it is possible to calculate a first-order approximation of the drag (Levich 1948). In principle, it is straightforward to obtain such a solution; however, the geometry poses some algebraic challenges. The symmetry of the problem will allow us to obtain an approximation from the equivalent geometry of a set of aligned spheres, separated by a regular distance R. The symmetry planes located at the middle of each pair of spheres are equivalent to the confining plane walls.

The technique employed for the solution of Laplace's equation is the same as that used by Kumaran & Koch (1993) where the velocity potential is initially set as an infinite series expansion of spherical harmonics. The coefficients of the series are then obtained by imposing the boundary conditions.

To construct this approximation, a sphere of radius a is placed at the origin, with two image spheres aligned along a common axis crossing through their centres. This arrangement produces a potential function equivalent to that of a sphere confined between two planes; note that the apparent planes of symmetry between the spheres (see figure 12) are not proper planes of symmetry. Proper planes of symmetry could be found if an infinite arrangement of spheres aligned along the same axis is considered. This case is discussed below (§ A. 2).

A. 1. *Three spheres aligned perpendicular to the flow*

Let us first obtain the potential for three aligned spheres. Consider an arrangement of three spheres of radius a, aligned along the fixed axis z, the origin being at the centre of the second sphere, as shown in figure 12. The radial and azimuthal coordinates are θ_i and r_i, corresponding to a coordinate system placed at the centre of the sphere i. The three systems share the same meridional angle μ.

The velocities of the three spheres are the same, as are their radii. The bubble velocity is parallel to the x axis, represented by the vector $\boldsymbol{U} = U\boldsymbol{e}_x$.

Let us assume a solution of the form

$$\phi = Ua\sum_{n=1}^{\infty}\left\{B_n^1\left(\frac{a}{r_1}\right)^{n+1}P_n^1(\cos\theta_1) + B_n^2\left(\frac{a}{r_2}\right)^{n+1}P_n^1(\cos\theta_2) + B_n^3\left(\frac{a}{r_3}\right)^{n+1}P_n^1(\cos\theta_3)\right\}\cos\omega, \quad \text{(A 1)}$$

where $r_1, r_2, r_3, \theta_1, \theta_2, \theta_3$ are the three bubble radii and polar angles, according to figure 12.

Since the velocity decreases to zero at large distances from the bubbles, only the decaying harmonics are retained and the potential is expressed as a function of the bubble separation and velocities. The constants B_n^1, B_n^2 and B_n^3 will be obtained by substitution in the no-penetration boundary condition

$$\frac{\partial\phi}{\partial r_i}|_{r_i=a} = U\sin\theta_i, \quad \text{(A 2)}$$

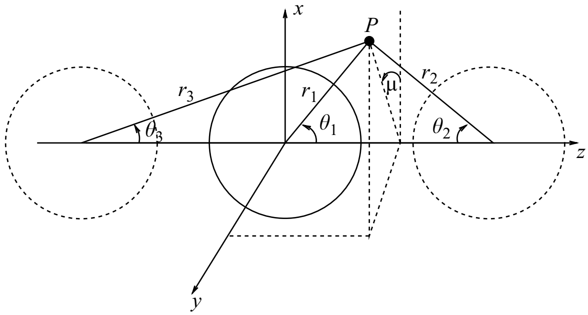

FIGURE 12. Bubble with two images and corresponding spherical coordinates.

where the projection of the bubble velocity on the normal vector of the surface has been calculated using the radial velocity in spherical coordinates, and the subscript i represents the surface of the bubble i, for the values $i = 1, 2, 3$.

This velocity potential is defined in terms of three different sets of coordinate systems $(r_i, \theta_i, \omega;\ i = 1, 2, 3)$. Depending on the boundary conditions to be satisfied at the surface of each bubble i, it is necessary to express the potential as a function of the corresponding set of variables (centred at the origin i). To do this, the series expansion derived by Hobson (1931) can be used:

$$\left(\frac{1}{r_i}\right)^{n+1} P_n^m(\cos\theta_i) = \left(\frac{1}{R}\right)^{n+1} \sum_{q=m}^{\infty} \binom{n+q}{q+m} \left(\frac{r_j}{R}\right)^q P_q^m(\cos\theta_j), \tag{A 3}$$

which is valid for any angles i, j opposite to each other, as is the case for the angles θ_1 and θ_2 in figure 12, for $r_j < R$. For angles with the same orientation (θ_1 and θ_3), an equivalent expression must be obtained as follows: consider the angle $\theta_4 = \pi - \theta_1$. Since this angle is opposite to θ_3, (A 3) can be used:

$$\left(\frac{1}{r_1}\right)^{n+1} P_n^m(\cos\theta_4) = \left(\frac{1}{R}\right)^{n+1} \sum_{q=m}^{\infty} \binom{n+q}{q+m} \left(\frac{r_3}{R}\right)^q P_q^m(\cos\theta_3), \tag{A 4}$$

where

$$\cos\theta_1 = -\cos\theta_4, \tag{A 5}$$

since θ_1 and θ_4 are supplementary angles.

Now, introducing the parity property (Arfken 1995)

$$P_q^m(\cos\theta) = (-1)^{(m+q)} P_q^m(-\cos\theta) \tag{A 6}$$

and replacing (A 5) and (A 6) in the left-hand side of (A 4), we have

$$\left(\frac{1}{r_1}\right)^{n+1} P_n^m(\cos\theta_1) = \left(\frac{1}{R}\right)^{n+1} \sum_{q=m}^{\infty} \binom{n+q}{q+m} \left(\frac{r_3}{R}\right)^q (-1)^{n+1} P_q^m(\cos\theta_3). \tag{A 7}$$

For the case of r_3, θ_3 as a function of r_1, θ_1 it can be shown, using the same procedure, that the factor introduced is $(-1)^{q+1}$.

Substitution of (A 1) and (A 3) into (A 2), for $i=1,2,3$ leads to

$$Ua\sum_{n=1}^{\infty}\left\{-B_n^1(n+1)+\sum_{q=1}^{\infty}\left(B_q^2+(-1)^{(n+1)}B_q^3\right)\binom{n+q}{n+1}q\left(\frac{a}{R}\right)^{n+q+1}\right\}Y_n^1(\theta,\omega) = U\delta_{1n}Y_n^1(\theta,\omega), \qquad (\mathrm{A}\,8)$$

$$Ua\sum_{n=1}^{\infty}\left\{-B_n^2(n+1)+\sum_{q=1}^{\infty}\left(B_q^1+\frac{B_q^3}{2^{n+q+1}}\right)\binom{n+q}{n+1}q\left(\frac{a}{R}\right)^{n+q+1}\right\}Y_n^1(\theta,\omega) = U\delta_{1n}Y_n^1(\theta,\omega), \qquad (\mathrm{A}\,9)$$

$$Ua\sum_{n=1}^{\infty}\left\{-B_n^3(n+1)+\sum_{q=1}^{\infty}\left((-1)^{q+1}B_q^1+\frac{B_q^2}{2^{n+q+1}}\right)\binom{n+q}{n+1}q\left(\frac{a}{R}\right)^{n+q+1}\right\} \times Y_n^1(\theta,\omega) = U\delta_{1n}Y_n^1(\theta,\omega), \qquad (\mathrm{A}\,10)$$

where s is the ratio a/R, a is the bubble radius, R is the distance between the centres of the spheres and $Y_n^1(\theta,\omega)=P_n^1(\cos\theta_1)\cos\omega$ (repeated indexes do not sum).

The double sums in n and q allow us to interchange indexes, such that each side of every equation can be expressed as a function of harmonics of the same order and degree, and the following equations could be derived:

$$-B_n^1+\sum_{q=1}^{\infty}\left(B_q^2+(-1)^{(n+1)}B_q^3\right)\frac{n}{n+1}\binom{n+q}{n+1}s^{n+q+1}=\frac{\delta_{1n}}{2}, \qquad (\mathrm{A}\,11)$$

$$-B_n^2+\sum_{q=1}^{\infty}\left(B_q^1+\frac{B_q^3}{2^{n+q+1}}\right)\frac{n}{n+1}\binom{n+q}{n+1}s^{n+q+1}=\frac{\delta_{1n}}{2}, \qquad (\mathrm{A}\,12)$$

$$-B_n^3+\sum_{q=1}^{\infty}\left((-1)^{(q+1)}B_q^1+\frac{B_q^2}{2^{n+q+1}}\right)\frac{n}{n+1}\binom{n+q}{n+1}s^{n+q+1}=\frac{\delta_{1n}}{2}. \qquad (\mathrm{A}\,13)$$

Now, for each value n, the set of linear equations (A 11)–(A 13) establishes the conditions that must be satisfied by the constants $B_{1,2,3\ldots}^{1,2,3}$ to give a solution that is consistent with the Laplace's equation and the boundary conditions given by (A 2). An approximate solution of $(n\times q)$ equations with $(n\times q)$ unknowns can be reached if the sums for n and q are truncated, starting from the value 1 to some positive real integers n and q, respectively.

The first approximation for the potential function of $O(s^3)$ requires $n=1$, $q=1$. Therefore,

$$-B_1^1+\left(B_1^2+B_1^3\right)\frac{1}{2}s^3=\frac{1}{2}, \qquad (\mathrm{A}\,14)$$

$$-B_1^2+\left(B_1^1+\frac{B_1^3}{2^3}\right)\frac{1}{2}s^3=\frac{1}{2}, \qquad (\mathrm{A}\,15)$$

$$-B_1^3+\left(B_1^1+\frac{B_1^2}{2^3}\right)\frac{1}{2}s^3=\frac{1}{2}. \qquad (\mathrm{A}\,16)$$

Then, the values of $B_1^{1,2,3}$ can be readily obtained as follows:

$$B_1^1=-\frac{1}{2}\frac{(s^3-16)}{(8s^6+s^3-16)}+8\frac{s^3}{(8s^6+s^3-16)}, \qquad (\mathrm{A}\,17)$$

$$B_1^2 = 4\frac{s^3}{(8s^6+s^3-16)} - 32\frac{(-4+s^6)}{(-256+129s^6+8s^9)} + 8\frac{s^3(1+4s^3)}{(-256+129s^6+8s^9)}, \tag{A 18}$$

$$B_1^3 = B_1^2. \tag{A 19}$$

The constants B_i^j are dependent on the a/R ratio, in a rather complicated manner, as can be seen from this first approximation. Equations (A 17)–(A 19) will be used in Appendix A. 2 to obtain the first-order terms for the drag coefficient. The constants, expressed as series of s, are

$$B_1^1 = -\frac{1}{2} - \frac{1}{2}s^3 - \frac{9}{32}s^6 + O(s^9), \tag{A 20}$$

$$B_1^2 = -\frac{1}{2} - \frac{9}{32}s^3 - \frac{137}{512}s^6 + O(s^9), \tag{A 21}$$

$$B_1^3 = B_1^2. \tag{A 22}$$

A. 2. *The drag as an infinite series of* $O(s^n)$

Now, since the potential is known, a first-order approximation to the drag can be obtained. Note that in (A 1), each of the lateral potentials must be evaluated in terms of the radius r_1 (and angle θ_1) to apply the boundary conditions in (A 2). For that purpose the relation (A 3) is used to obtain

$$\phi = Ua\sum_{n=1}^{\infty}\left\{B_n^1\left(\frac{a}{r_1}\right)^{n+1} P_n^1(\cos\theta_1) + \left(B_n^2 + B_n^3\right)\left(\frac{1}{R}\right)^{n+1} \times \sum_{q=m}^{\infty}\binom{n+q}{q+m}\left(\frac{r_1}{R}\right)^{q} P_q^m(\cos\theta_1)\right\}\cos\omega. \tag{A 23}$$

The velocity field is obtained by performing the derivatives of the potential function:

$$v_r = \frac{\partial\phi}{\partial r_1}, \tag{A 24}$$

$$v_\theta = \frac{1}{r_1}\frac{\partial\phi}{\partial\theta_1}, \tag{A 25}$$

$$v_\omega = \frac{1}{r\sin\theta}\frac{\partial\phi}{\partial\omega}, \tag{A 26}$$

$$v_f^2 = v_r^2 + v_\theta^2 + v_\omega^2. \tag{A 27}$$

Based on the analysis of Levich (1948), to obtain the drag force the following surface integral has to be calculated:

$$\boldsymbol{F}_D\boldsymbol{\cdot}\boldsymbol{U} = -\mu\int_V \varDelta(\boldsymbol{u}_f\boldsymbol{u}_f)\mathrm{d}V = -\mu\int_A \frac{\partial u_f^2}{\partial x_j}n_j\,\mathrm{d}A, \tag{A 28}$$

where $\boldsymbol{U}$ is the bubble velocity.

The dimensionless drag force or drag coefficient, C_D, is normalized by $C_{D\,Levich} = 48/Re$ to obtain

$$C_D^* = \frac{C_D}{C_{D\,Levich}} = 4\left(B_1^1\right)^2 + 24\left(B_1^2\right)^2 + 16\left(B_2^1\right)^2 s^8 + 128B_2^1B_2^2s^9 + \cdots. \tag{A 29}$$

For the special case of a single bubble, $B_1 = 0.5$, $s = 0$ and $B_{2,3}^i = 0; \forall i$, the result of Levich is recovered.

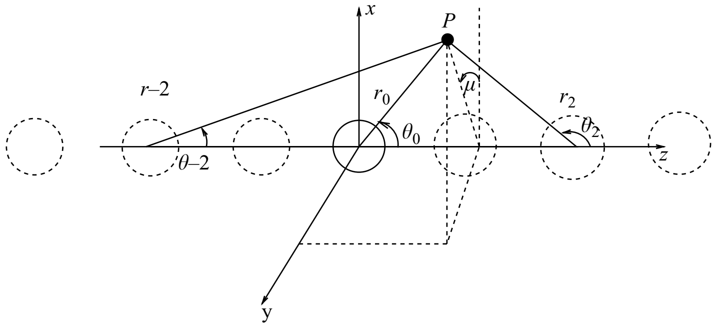

FIGURE 13. Infinite array of spheres. The one in the origin is number 0, and increasing positive and negative indexes appear to the right and left respectively.

The expression (A 29) can be expanded in a Taylor series as a function of s to obtain

$$C_D^* = 1 + 2s^3 + \frac{17}{8}s^6 + O(s^8) + \cdots . \tag{A 30}$$

Equation (A 30) can be compared with the result obtained by Kok (1993) for the drag in the case of two bubbles side-by-side in potential flow as:

$$\frac{C_D}{C_{D\,Levich}} = 1 + s^3 + \frac{3}{4}s^6 + O(s^9) + \cdots . \tag{A 31}$$

Interestingly, the leading order term is exactly twice that of the bubble pair case. The validity of this expression is expected to improve as $s \to 0$. Although (A 30) may not be a good approximation for $s \to 0.5$, expression (A 29) can be used, since the values for B_i^j can be calculated numerically for any i, j. Therefore, it is possible, in principle, to improve the precision of (A 30).

A. 3. *Infinite array of spheres aligned perpendicular to the flow*

The generalization to consider an infinite set of horizontally aligned bubbles is straightforward. Let us consider the same geometry as in the previous case, being the centre bubble indexed with the number zero, the next bubble to the right would be bubble one, the one to the left being bubble minus one, etc., as is shown in figure 13.

The procedure is the same as in the previous case, starting from a potential of the same form, with spherical harmonics centred at each bubble:

$$\phi = Ua\sum_{n=1}^{\infty}\left\{\sum_{k=1}^{\infty} B_n^k \left(\frac{a}{r_k}\right)^{n+1} P_n^1(\cos\theta_1)\right\}\cos\omega, \tag{A 32}$$

where the index k represents the corresponding image sphere, having a spherical harmonic of order n associated with it.

It is possible to obtain the equations for the corresponding constants at bubble i:

$$-B_n^i = \frac{1}{2}\delta_{1n} - \frac{n}{n+1}\sum_{k\neq i}\sum_{q=1}^{\infty}\binom{n+q}{n+1} s^{q+n+1}\frac{B_q^k}{|i-k|^{n+q+1}}\xi_{ik}, \tag{A 33}$$

where

$$\xi_{ik} = \begin{cases}(-1)^{n+1}, & k < i,\\ (-1)^{q+1}, & k > i.\end{cases} \tag{A 34}$$

This is, again, a linear set of $(n \times q)$ equations with the same number of unknowns. The velocity field resulting from this solution has two proper planes of symmetry at each side of the central bubble $(i = 0)$. If the calculation is truncated to a reasonable number of lateral bubbles, such planes of symmetry would be equivalent to plane walls. The three bubbles problem of the previous section is the case of having only the bubbles −1, 0 and 1, which can be recovered by direct substitution in (A 33). Note that if an infinite arrangement of dipoles is considered, the additive effect on the drag would give $1 + 2s^3(1 + 1/2^3 + 1/3^3 + 1/4^3 + \cdots)$. Therefore, the confinement correction on the drag force would be

$$f(s) = 1 + 2\zeta(3)s^3 + \cdots = 1 + 2.4s^3 + \cdots, \tag{A 35}$$

where ζ is the Riemann Zeta-function.

REFERENCES

Arfken, G. B. & Weber, H. J. 1995 *Mathematical Methods for Physicists.* Academic Press.

Bairstow, L., Cave, B. M. & Lang, E. D. 1922 The two-dimensional slow motion of viscous fluids. *Proc. R. Soc. Lond.* A **705**, 394.

Biesheuvel, A. & van Wijngaarden, L. 1982 The motion of pairs of gas bubble in a perfect liquid. *J. Engng Math.* **16**, 349–365.

Brücker C. 1999 Structure and dynamics of the wake of bubbles and its relevance for bubble interaction. *Phys. Fluids* **11** (7), 1781–1796.

Clift, R., Grace, R. J. & Weber, M. E. 1978 *Bubbles, Drops and Particles.* Academic Press.

De Vries, A. W. G. 2001 Path and wake of a rising bubble. PhD thesis, University of Twente, the Netherlands.

Duineveld, P. C. 1995 The rise velocity and shape of bubbles in pure water at high Reynolds number. *J. Fluid Mech.* **292**, 325–332.

Faxen, H. 1922 Der widerstand gegen die bewegung einer starren kugel in einer zahen flussigkeit, die zwischen zwei parallen ebenen wanden eingeschlossen ist. *Ann. Phys.* **68**, 89.

Hadamard, J. 1911 Mouvement permanent lent dune sphere liquide et visqueuse dans un liquide visqueux *C. R. Acad. Sci. Paris* **152**, 1735.

Happel, J. & Brenner, H. 1991 *Low Reynolds Number Hydrodynamics.* Kluwer.

Hobson, E. W. 1931 *The Theory of Spherical and Ellipsoidal Harmonics.* Cambridge University Press.

Kok, J. B. W. 1993 Dynamics of a pair of gas bubbles moving through liquid. Part I. Theory. *Eur. J. Mech.* B *Fluids* **12**, 515–540.

Kumaran, V. & Koch, D. L. 1993 The effect of hydrodynamic interactions on the average properties of a bidisperse suspension of high-Reynolds-number, low Weber number bubbles. *Phys. Fluids* **5**, 1123–1134.

Legendre, D. & Magnaudet, J. 1998 The lift force on a spherical bubble in a viscous linear shear flow. *J. Fluid Mech.* **368**, 81–126.

Legendre, D., Magnaudet, J. & Mougin, G. 2003 Hydrodynamic interactions between two spherical bubbles rising side by side in a viscous liquid. *J. Fluid Mech.* **497**, 133–66.

Legendre, D. 2007 On the relation between the drag and the vorticity produced on clean bubble. *Phys. Fluids* **19**, 018102.

Levich, V. G. 1948 The motion of bubbles at high Reynolds numbers. *Zh. Eksptl. Teor. Fiz.* **19**, 18.

Levich, V. G. 1962 *Physico–Chemical Hydrodynamics.* Prentice Hall.

Magnaudet, J. & Mougin, G. 2007 Wake instability of a fixed spheroidal bubble. *J. Fluid Mech.* **572**, 311337.

Moctezuma, M. F., Lima-Ochoterena, R. & Zenit, R. 2005 Velocity fluctuations resulting from the interaction of a bubble with a vertical wall. *Phys. Fluids* **17**, 098106.

Moore, D. W. 1963 The boundary layer on a spherical gas bubble. *J. Fluid Mech.* **16**, 161–176.

Moore, D. W. 1965 The velocity of rise of distorted gas bubbles in a liquid of small viscosity. *J. Fluid Mech.* **23**, 749–766.

Mougin, G. & Magnaudet, J. 2002 Path instability of a rising bubble. *Phys. Rev. Lett.* **88**, 014502.

Rybczynski, W. 1911 Uber die Fortschreitende Bwegung einer-ussigen Kugel in einem zahen Medium. *Bull. Acad. Sci. Cracovie Ser.* A 1 **40**, 1.

Sato, A., Shirota, M., Sanada, T., Watanabe, M. & Ruzicka, M. 2007 Path and wake of a pair of bubbles rising side by side. In *Sixth International Conference on Multiphase Flow*, S1_Wed_D_45, Leipzig, Germany.

Shew, W., Poncet, S. & Pinton, J.-F. 2006 Force measurements on rising bubbles. *J. Fluid Mech.* **569**, 51–60.

Takemura, F. & Magnaudet, J. 2003 The transverse force on clean and contaminated bubbles rising near a vertical wall at moderate Reynolds number. *J. Fluid Mech.* **495**, 235–253.

Veldhuis, C. 2007 Leonardo's paradox: Path and shape instabilities of particles and bubbles. PhD thesis, University of Twente, the Netherlands.

van Wijngaarden, L. 1976 Bubble interactions between bubbles in liquid. *J. Fluid Mech.* **77**, 27–44.

Yang, B. & Prospereti, A. 2007 Linear stability of the flow past a spheroidal bubble. *J. Fluid Mech.* **582**, 53–78.

Zenit, R. & Magnaudet, J. 2008 Path instability of rising spheroidal air bubbles: a shape-controlled process. *Phys. Fluids* **20**, 061702.